



CHALMERS
UNIVERSITY OF TECHNOLOGY

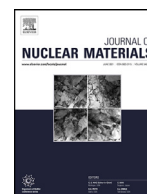
Performance and evolution of cold spray Cr-coated optimized ZIRLO™ claddings under simulated loss-of-coolant accident conditions

Downloaded from: <https://research.chalmers.se>, 2024-03-13 07:13 UTC

Citation for the original published paper (version of record):

Fazi, A., Sattari, M., Stiller, M. et al (2023). Performance and evolution of cold spray Cr-coated optimized ZIRLO™ claddings under simulated loss-of-coolant accident conditions. Journal of Nuclear Materials, 576.
<http://dx.doi.org/10.1016/j.jnucmat.2023.154268>

N.B. When citing this work, cite the original published paper.



Performance and evolution of cold spray Cr-coated optimized ZIRLO™ claddings under simulated loss-of-coolant accident conditions

Andrea Fazi*, Mohammad Sattari, Krystyna Stiller, Hans-Olof Andrén, Mattias Thuvander

Department of Physics, Chalmers University of Technology, SE-412 96 Gothenburg, Sweden



ARTICLE INFO

Article history:

Received 29 July 2022

Revised 16 December 2022

Accepted 11 January 2023

Available online 12 January 2023

Keywords:

Accident tolerant fuels

Cold spray Cr coating

Loss-of-coolant accident

High temperature steam oxidation

ABSTRACT

The performance of Cr-coated Optimized ZIRLO™ as accident tolerant fuel cladding material for pressurized water reactors (PWRs) is assessed. The coating oxidation mechanisms, oxide stability, and the transformation of the Cr-coating/Optimized ZIRLO™ interface are among the studied phenomena. For this purpose, samples were exposed at 1200°C in steam for 3 min, 20 min and 40 min. As-fabricated coated claddings, plus specimens tested in autoclave at 415°C for 90 days in simulated PWR water chemistry were employed for comparison. Characterization techniques such as scanning electron microscopy, energy dispersive x-ray spectroscopy, electron backscattered diffraction, and transmission electron microscopy were used to determine the chemistry and crystalline structure of the various phases formed during the different exposures. When exposed to loss-of-coolant accident (LOCA) conditions for 40 min, a layer of Cr₂O₃ up to 8 μm thick was measured on the outer surface of the Cr-coating. No significant oxidation of the underlying Optimized ZIRLO™ alloy occurred, and the applied coating appears to be very effective at delaying the cladding degradation under accident conditions. At the coating-substrate interface, a 1–2 μm thick layer of (Cr,Fe)₂Zr Laves phase was found. The presence of this phase appears to have no detrimental effects on the coating performance, and it might play a role in slowing down the dissolution of the coating into the substrate. ZrO₂ particles were frequently found at grain boundaries in the coating after exposure to LOCA conditions. For longer exposure time, these particles are expected to grow into a ZrO₂-network, creating a fast diffusion path for O, and compromising the oxidation protection offered by the coating.

© 2023 The Author(s). Published by Elsevier B.V.

This is an open access article under the CC BY license (<http://creativecommons.org/licenses/by/4.0/>)

1. Introduction

The main design objective of accident tolerant fuels (ATFs) is to greatly improve safety under severe accidents conditions. Loss-of-coolant accidents (LOCAs) are one of the most serious and consequential emergency situations that can occur in a nuclear power plant. In such accidents, the flow of water through the core is stopped. This could be the consequence of a loss of electric power to the pumps that drive the water into the core. From the instant when the water flow stops the core starts heating up, the temperature can quickly ramp up to 800°C where ballooning and burst of the cladding start occurring, followed by chemical degradation of the claddings and further increase in temperatures up to 1000–1200°C or more [1,2]. High temperature steam reacts with the zirconium metal, forming zirconium oxide and producing large quantities of hydrogen in a highly exothermic reaction [2]. Part of

the hydrogen is adsorbed by the zirconium cladding forming hydrides and further deteriorating the mechanical properties of the claddings, the rest is released as hydrogen gas into the core where it contributes to increasing the pressure inside the reactor vessel. This hydrogen gas can subsequently be released outside the containment due to reactor pressure vessel failure, ignite and cause explosions, further damaging the power plant and making it even more difficult to restart the flow of cooling water. All of this can happen in a matter of hours, and in these emergency situations any additional time is instrumental and could allow the personnel to react and solve the issue [1,2]. Cr-coatings are expected to be able to delay the reaction between hot steam and Zr-claddings. This would preserve the mechanical properties and the integrity of the claddings for longer time, which can guarantee a coolable geometry of the core and increase the time window where a severe accident can be contained by restarting the water flow before the situation becoming catastrophic. Also, delaying the oxidation of the Zr means delaying the injection of additional reaction heat in the core, reducing the rate at which the core temperature increases during the accident. Cr-coatings have been shown to perform well

* Corresponding author.

E-mail address: fazi@chalmers.se (A. Fazi).

both under pressurized water reactor (PWR) operating conditions and severe accident conditions [3–9], but a clear understanding of all phenomena and transformations occurring in the coating-cladding system during a severe accident is crucial for modelling the behaviour of the newly developed fuel.

Previous, in-depth studies on physical vapour deposition (PVD) Cr coatings for ATF have been performed [10–12], but a detailed chemical and microstructural analysis of cold spray (CS) Cr coatings tested under simulated accident conditions is still needed [5,9]. Metallic chromium has been selected for its ability to form a dense and protective chromia scale on its surface, both under operating conditions and during high temperature oxidation [5,13]. In most other applications, Cr is not used as a pure metal but added to steels or Ni-alloys as alloying element to provide improved oxidation/corrosion resistance [14–16]. The result is that these systems often oxidize producing a complex layered oxide scale composed of chromia and spinel oxides, which can promote chromia stability and protect it from dissolution and evaporation [16,17]. In the case of a coating made of pure Cr, the main solid oxidation product that can form is chromia and the performance of this oxide in the tested environment is crucial for the effectiveness of the coating in protecting the Zr-cladding. Under operating conditions, Cr forms a stable layer of passivating chromia [3–9], and its stability has been confirmed by thermodynamic calculations of Cr oxidation products under similar conditions conducted by Cook et al. [18]. In this case, the oxide grows through the diffusion of Cr-cations from the metal to the oxide surface where they react with H₂O and produce oxide growth [19]. At high temperature, the oxidation process can instead be described as the oxidation of the metal at the oxide-metal interface, plus the reduction of oxygen at the oxide-steam interface. Both phenomena are controlled by the diffusion of Cr vacancies from the outer surface to the metal and of O vacancies from the metal-oxide interface to the outer surface [20–23]. Depending on the environment the Cr is exposed to, the mobility of vacancies and the activity of oxygen can promote different oxidation mechanisms, kinetics, morphologies and microstructure of the oxide scale. Some of the most important exposure parameters for oxidation are temperature, O partial pressure and presence of steam [15,21,22,24–26]. Another issue worth keeping in mind is the thermal stability of Cr₂O₃. At temperatures higher than 1000–1200°C, chromium can start oxidizing into CrO₃ and other volatile species. These species have a significantly higher partial pressure than Cr₂O₃, can evaporate from the oxide surface, and can have an important role in the loss of protection against oxidation. [14,27,28].

Different ways of obtaining a metallic Cr coating exist: PVD and CS are currently the most widely used techniques for ATF applications [4,29,30]. In CS, high pressure, hot gas is fed through a converging-diverging nozzle together with a powder. The powder particles represent the building blocks that will assemble into the final coating. After passing through the nozzle, the powder is accelerated by the expanding gas up to supersonic speed (the achieved particle velocity usually falls between 300 m/s and 1200 m/s [31,32]). The accelerated particles are then directed onto the substrate, where they undergo ballistic collision with the substrate, to start with, and subsequently with the coating being formed. The impact of the particles results in high-strain, high-rate plastic deformation, where kinetic energy provides the principal driving force for coating consolidation and particle adhesion [32]. In this work, scanning electron microscopy (SEM), energy dispersive x-ray spectroscopy (EDS), transmission electron microscopy (TEM), and electron backscattered diffraction (EBSD) are employed to study CS Cr-coated Zr-claddings exposed to a simulated accident environment. This material is analysed in search of an understanding of the Cr oxidation mechanism, the interaction between the Cr-coating and the Zr-substrate at elevated tempera-

tures, and the microstructural and chemical evolution of the system under these challenging conditions. Analysis and results from as-fabricated coated cladding and PWR autoclaved coated cladding are also used for comparison and for understanding the origin of the microstructure and phases that emerge after the exposure to simulated LOCA conditions.

2. Experimental procedures

2.1. Materials

Cold spray Cr-coated Optimized ZIRLO™ (OPZ) cladding material, in form of tubes 4 cm long and 10 mm in diameter, is analysed. The coating was obtained by depositing pure Cr powder sieved to less than 44 µm in size with CS deposition (achieved particle velocity 1200 ± 50 m/s) onto OPZ cladding tubes (4 m long; alloy nominal composition: 0.8–1.2 wt.% Nb, 0.6–0.79 wt.% Sn, 0.09–0.13 wt.% Fe, 0.09–0.16 wt.% O, balance Zr). Initially, 50 µm of coating was deposited, then the coating was machined down to 20 µm thickness. This step guarantees better control on coating thickness and surface roughness. The coated tubes were cut into 4 cm long portions, and these smaller specimens were exposed to simulated PWR operating conditions and simulated LOCA conditions. The simulated PWR exposure was performed in a closed loop, static, steam autoclave at 415°C and 220 bar for a total of 90 days in PWR water-chemistry. Static steam autoclave testing on Zr-alloys is generally performed at 400°C [33], the slightly higher temperature of 415°C was used in this study to test the material under harsher conditions. A horizontal quartz tube furnace with 1 atm flowing steam was used to simulate the accident conditions. The tube samples were inserted into the furnace, pre-heated at 1200°C, once the target temperature was reached, the samples were held inside for 3 min, 20 min and 40 min, respectively. After the exposure was completed, the samples were extracted from the furnace and let to cool in air. A type-K thermocouple was spot welded to a dummy Zr-alloy tube sample and used to monitor the temperature inside the furnace. The dummy was kept adjacent to the actual sample for the duration of the experiment.

2.2. Sample preparation and analysis

A low-speed saw was used to cut the received samples into rings 5 mm in height. Bakelite embedded samples, ground and polished with SiC-paper and diamond particle suspensions, were subjected to SEM study and EDS analysis. Cross-sections prepared with broad ion beam (BIB) LEICA TIC3X were employed for EBSD mapping of as-fabricated material and PWR-autoclave exposed samples. EBSD mapping of the LOCA tested material was performed on the ground and polished Bakelite embedded samples. TEM specimens were extracted from the Bakelite-embedded samples with a dual-beam focused ion beam/scanning electron microscope (FIB/SEM) in an FEI Versa 3D workstation implementing well-known procedures for sample lift-out and preparation [34,35]. SEM and EDS analyses were conducted on a JEOL 7800F Prime microscope, providing an overview of the morphology and the microstructure. EBSD mapping (band contrast and inverse pole figure (IPF)) was performed on a TESCAN GAIA3 equipped with an Oxford-NordlysNano detector and used to study the microstructural evolution of the coating during autoclave and under simulated accident conditions. In the case of the LOCA tested sample (40 min), bright field (BF)-TEM images and selected area diffraction patterns (SADPs) were collected on an FEI Tecnai T20 LaB₆, while scanning TEM (STEM) imaging and STEM-EDS analyses were performed on an FEI Titan 80-300 FEG. The combination of the two instruments was used to identify and characterize the oxide scale, the (Cr,Fe)₂Zr Laves phase formed at the Cr/Zr interface, and the ZrO₂ particles formed in the coating

at the Cr grain boundaries in proximity of the interface with the substrate.

3. Results

3.1. Oxidation protection under simulated accident environment

An overview of the performance of the coated cladding after hot steam testing is presented in Fig. 1. After exposure, the coated outer wall of the cladding is still protected by the coating. Three main features can be observed; a compact oxide scale has formed on the surface, an intermetallic $(\text{Cr,Fe})_2\text{Zr}$ Laves phase has appeared at the Cr/Zr interface, and some pores both in the oxide and the coating can be observed. Looking at the evolution in time, it can be noticed that the thickness of the oxide scale and of the Laves phase increase visibly between 3 min and 20 min, while not much difference is noticeable between 20 min and 40 min. As can be seen in Box 1, in the initial stages of oxidation (LOCA 3 min), the oxide scale is uniform and monolithic, characterized by crystallites around $100\text{ nm} \times 200 - 300\text{ nm}$ in size (elongated along the growth direction). At this stage the interface with the Cr-coating appears to contain many pores with localized points of contact between the scale and the metal, compatible with an initial outward growing oxide. For longer exposure time, the oxide grows in thickness and the interface with the metal changes morphology and no pores can be observed any longer. The oxidation mechanism becomes mixed, the oxide is both outward growing and inward growing, leading to the incorporation of the original oxide/metal interface inside the oxide scale. Overall, the result of the exposure to LOCA simulated conditions for 40 min is the formation of a passivating chromia scale $8-10\text{ }\mu\text{m}$ thick with no severe damage to the

integrity of the coating. When compared with the degree of oxidation suffered by the uncoated inner wall of the cladding (shown in Fig. 1b), the advantage provided by the coating is immediately clear. Where uncoated, the Zr-alloy produced an $80\text{ }\mu\text{m}$ thick ZrO_2 scale plus more than $100\text{ }\mu\text{m}$ of oxygen saturated $\alpha\text{-Zr(O)}$.

The thickness of the chromium oxide and the $(\text{Cr,Fe})_2\text{Zr}$ Laves phase developed during exposure to simulated accident environment were measured for the three different times, see Fig. 2. The thicknesses were measured along a $150\text{ }\mu\text{m}$ long portion of the cladding outer wall, by analysing cross-section SEM images. As can be seen, both the oxide and the Laves phase appear to grow following a parabolic kinetics and can be well fitted by a parabolic law. Another interesting detail shown by this plot is the reduced spread of measured thicknesses for the Laves phase after 40 min relative to 20 min. As confirmed by Fig. 1, over time, the coating-substrate interface tends to become less rough and more homogeneous, and this could have an effect on the Laves phase thickness homogeneity.

Due to the mechanical polishing, the oxide scale visible in Fig. 1 appears to be incomplete. A complete view on the chromia scale formed after 40 min under simulated LOCA conditions is offered in Fig. 3. In this BF-TEM micrograph the entirety of the scale, from the outer surface to the interface with the metal, is presented. The scale can be divided into two separate bands: an outer one characterized by small grains (less than 100 nm in size), and an inner one where the grains are larger ($0.5-1\text{ }\mu\text{m}$ in size) and many pores can be found. The transition from one region to another is gradual and in the central zone of the scale, large grains can be found surrounded by many smaller ones. The oxide/metal interface appears to be continuous, and no porosity or lack of material can be seen. Some small circular pores are found in the Cr

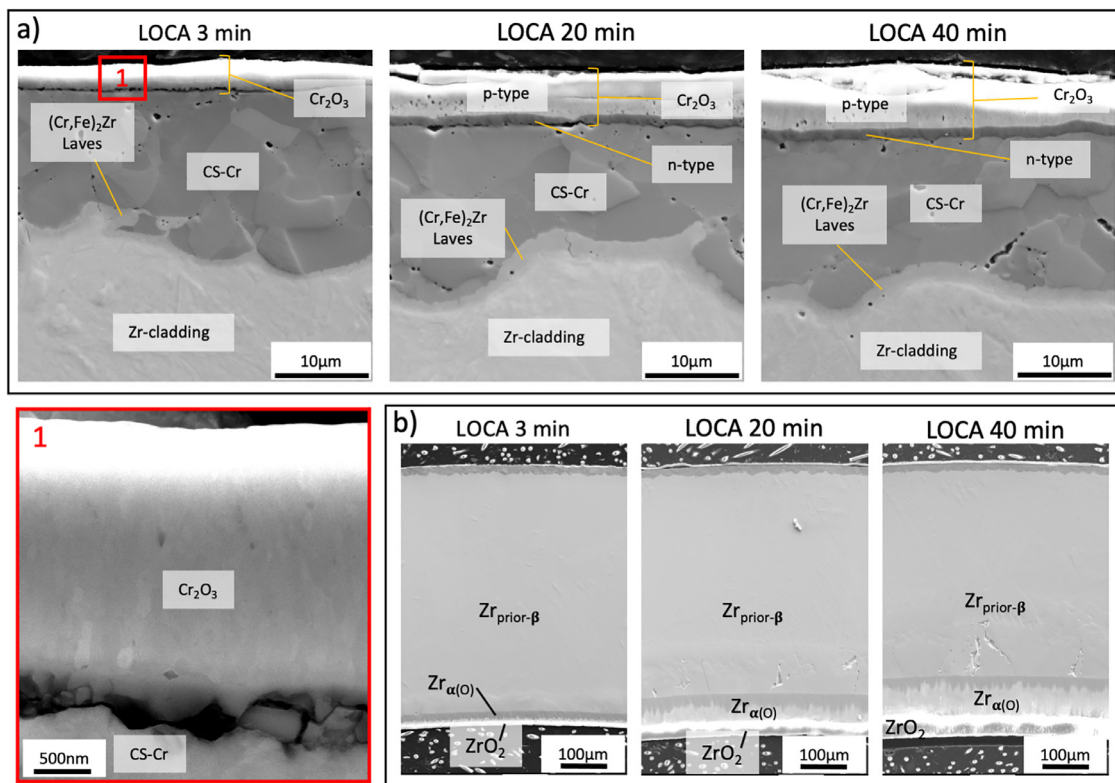


Fig. 1. SEM cross-section imaging of CS Cr-coated OPZ cladding tubes exposed to LOCA condition (1200°C in steam) for 3 min, 20 min and 40 min respectively. (a) Detail of the outer cladding wall, Cr-coated, after exposure. Due to the different electronic properties, n-type and p-type chromia present different contrast. Box 1 offers a magnified view of the oxide scale and the oxide/metal interface after 3 min of exposure. (b) Overview of the cladding cross-section: the uncoated inner wall of the cladding is shown and the degree of oxidation suffered by the bare Zr-alloy is visible.

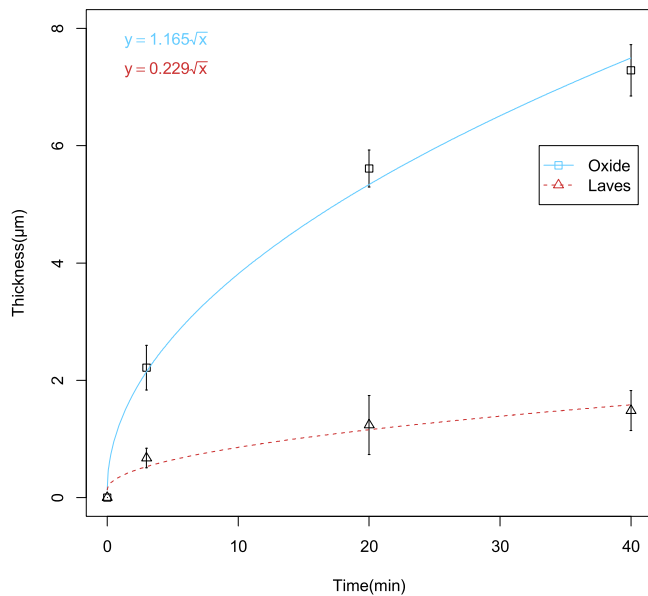


Fig. 2. Thickness of the chromium oxide scale and the $(\text{Cr,Fe})_2\text{Zr}$ Laves phase layer measured after exposure to simulated LOCA conditions. The fitted parabolic law curves are plotted as solid lines.

grains visible in this region near the oxide, which could be explained as Kirkendall porosities [11,36]. The electron diffraction pattern A (Fig. 3) is compatible with the ring patterns produced by a multi-crystalline chromia, but the number of grains included in the selected area for electron diffraction was not sufficient to produce complete rings. Pattern B was successfully indexed as trigonal chromia, and Pattern C was indexed as BCC-Cr.

3.2. Cr-Zr interdiffusion at the coating-substrate interface

Another region of interest, which is subjected to transformation during the exposure at high temperature, is the Cr-Zr interface. Fig. 4 offers an EDS map comparison between the as-fabricated material, the PWR autoclaved material and the LOCA tested material. The Cr-Zr interface appears sharp for the as-fabricated and PWR autoclaved samples, while an intermixing between Cr and Zr can be noticed in the case of the LOCA tested samples. In fact, the most evident phenomenon occurring at the interface once high temperatures are involved is the formation of a 1–2 μm thick layer of intermetallic Laves phase $(\text{Cr,Fe})_2\text{Zr}$. The $(\text{Cr,Fe})_2\text{Zr}$ Laves phase is 0.5 μm thick after 3 min of high temperature exposure and it grows to around 1–1.5 μm after 20 min. At this point the thickness of this phase seems to stabilize. The EDS maps presented in Fig. 4 allow to see a vague trend in the presence of Fe in the Laves phase: no visible Fe enrichment after 3 min, initial stages of Fe enrichment after 20 min and clear Fe enrichment after 40 min. The concentration of Fe in the Laves phase after 40 min is still very low, probably around 1–2 at.%, which makes it difficult to highlight clearly with SEM-EDS mapping. Better quantification is offered in Fig. 7b where the results from STEM-EDS point analysis is presented. A trend can be seen for the thickness of the outer oxide as well, no oxide is visible at this magnification for the as-fabricated material, a very thin scale is identified on the PWR autoclaved material, a 2–3 μm thick oxide layer is measured after 3 min of LOCA exposure, and an 8 μm oxide layer can be seen after 20 min with little increase in thickness after 40 min. Beyond the formation of the oxide and the intermetallic, it is possible to see some Zr signal inside the Cr-coating forming a network of loosely interconnected lines, most likely Zr is diffusing along grain boundaries into the coating. No Zr was measured in the bulk of the Cr grains (notice: the detection limit of EDS is about 0.1–0.2 at.%). Due to the depo-

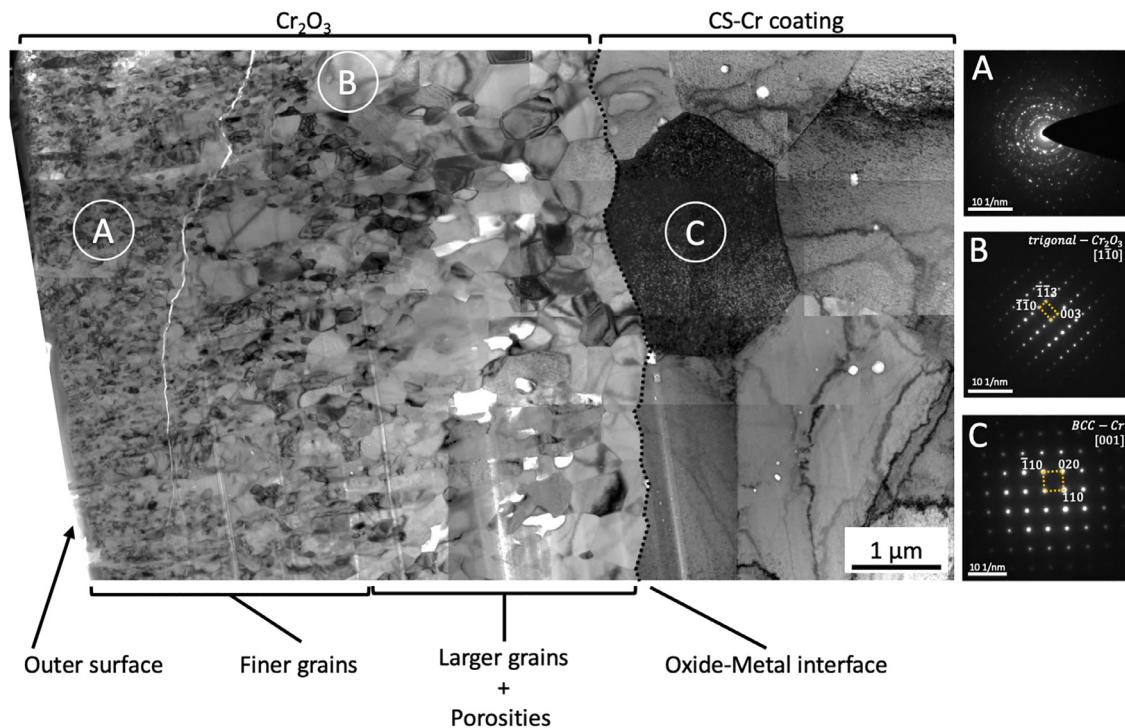


Fig. 3. BF-TEM image of the chromia scale formed on the outer surface of the CS Cr-coated OPZ cladding tube after 40 min at 1200°C in steam (montage of multiple images). Right: SADPs from (A) multiple grains of chromia in the outer part of the oxide scale, (B) single grain of chromia midway through the oxide scale, (C) single grain of Cr metal adjacent to the oxide scale.

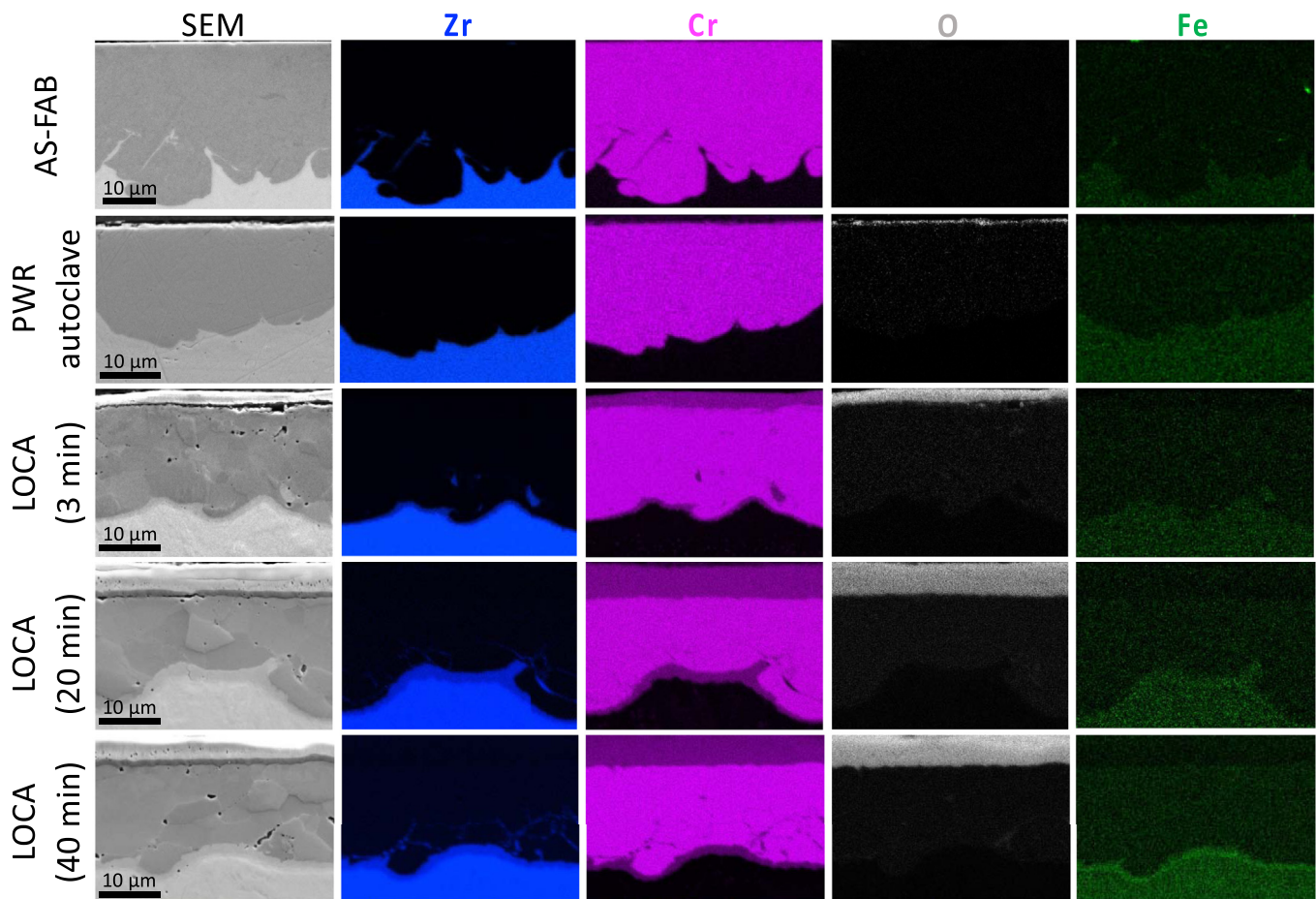


Fig. 4. SEM EDS cross-section mapping of CS Cr-coated OPZ cladding tubes as-fabricated, exposed to PWR autoclave, and exposed to LOCA condition (1200°C in steam) for 3 min, 20 min and 40 min, respectively. (Mapped elements: Zr in blue, Cr in magenta, O in grey, Fe in green. SEM images with scale bar shown in left column).

sition method and the consequent roughness of the Cr-Zr interface, some Zr could already be measured penetrating the coating in the as-fabricated or PWR autoclaved samples. This, though, was caused by the turbulent flow of plastically deformed material that characterizes CS deposition. It could be seen only in certain regions and with only nanometre scale chemical intermixing at the interface, showing significantly different characteristics [37,38].

Chromium diffused into the bulk of the Zr cladding in significant amounts, as shown in Fig. 5. Utilizing SEM EDS line scans, it was possible to quantify the Cr diffusion into the Zr cladding. No Cr has diffused into the Zr cladding for the as-fabricated sample as the low deposition temperature of cold spray deposition does not allow for long range diffusion to happen. During PWR autoclave testing, despite the relatively low exposure temperature of 415°C, due to the long exposure time of 90 days, a small degree of Cr diffusion with a range of 8–10 µm was measured. The Cr content for the LOCA tested samples is more significant, here the Cr concentration adjacent to the Cr coating peaks at 5 at.% for all exposure times. From this point, moving towards the inner wall of the coating, the Cr content decreases to reach zero approximately at 75 µm, 200 µm, and 300 µm distance from the coating-substrate interface for the 3 min, 20 min and 40 min LOCA exposures, respectively. The box on the right side of Fig. 5 shows a schematic example of the position and direction of the SEM EDS line scans collected. Additionally, the mapped EDS signal for Cr inside the Zr cladding is presented. From this it is possible to see that, after the exposure at 1200°C and cooling in air at room temperature, Cr is not uniformly distributed in the Zr alloy. Both micron sized Cr-rich

particles and Cr-rich areas can be found in the Zr. These two features, typical of Zr alloys containing 3 at.% Cr or more [39], are the cause behind the fluctuation of the Cr content measured in the line scans. The plotted data was obtained by aligning and averaging five line scans per sample in an attempt to reduce the compositional fluctuations characteristic of the LOCA exposed samples in particular, but the magnitude of these fluctuation made it very difficult to obtain a smooth curve. It is also important to notice that the $(\text{Cr,Fe})_2\text{Zr}$ Laves phase band, present at the Cr-Zr interface for all three samples exposed in LOCA simulated environment, it is not visibly plotted in Fig. 5 due to the scaling of the axis.

A better view of the Cr-Zr interface after 40 min exposure in simulated LOCA environment is presented in Fig. 6a. On the Cr-side, bright particles can be seen at the grain boundaries of the recrystallized Cr grains. These particles correspond to the Zr-rich regions penetrating into the Cr-coating that are visible in the EDS map presented in Fig. 4. Between the Cr and the Zr, the $(\text{Cr,Fe})_2\text{Zr}$ Laves phase layer appears to have sharp interfaces with both materials, the interfaces have some roughness but the thickness of the intermetallic is relatively uniform. On the Zr side, the aforementioned Cr-rich particles are found with both elongated/acicular shapes and spherical shapes. The region of Zr within 1–2 µm distance from the intermetallic Laves phase does not present any of these particles. This could be due to a Cr depletion zone produced by the growth of the $(\text{Cr,Fe})_2\text{Zr}$ layer at the coating-substrate interface. BF-TEM images of the Cr- $(\text{Cr,Fe})_2\text{Zr}$ interface is shown in Fig. 6b. In addition to the features already visible in the SEM cross-section, TEM allows to partially access the $(\text{Cr,Fe})_2\text{Zr}$ grain struc-

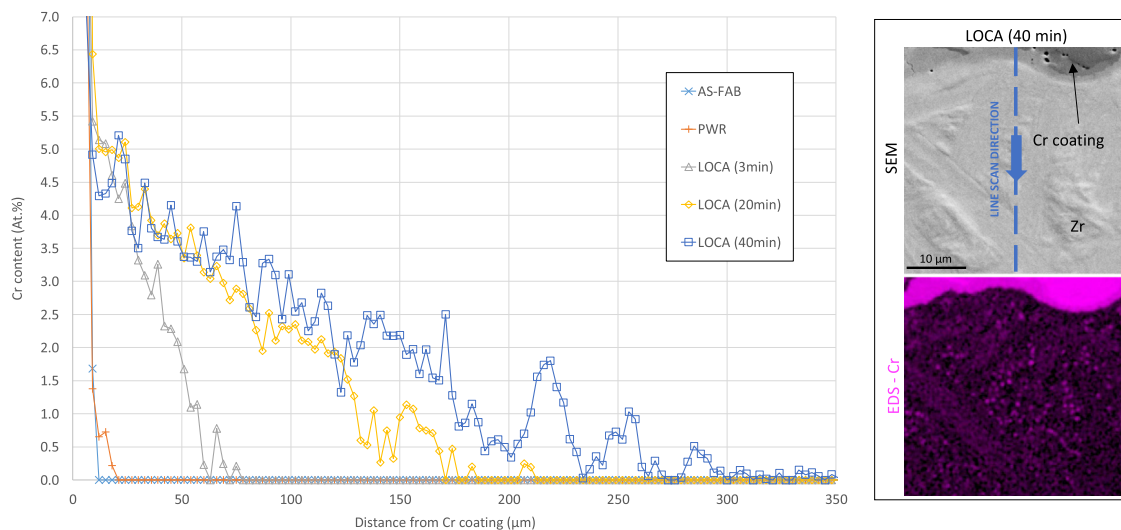


Fig. 5. SEM EDS cross-section line scans of CS Cr-coated OPZ cladding tubes as-fabricated, exposed to PWR autoclave, and exposed to LOCA condition (1200°C in steam) for 3 min, 20 min and 40 min respectively. Box (right side): Schematic of line scan direction and orientation, plus SEM EDS map of the Cr signal from the Zr cladding (signal intensity adjusted to make Cr-rich particles and regions visible – contrast between the $(\text{Cr,Fe})_2\text{Zr}$ Laves and the Cr-coating is not visible due to oversaturation).

ture. Near the interface, $(\text{Cr,Fe})_2\text{Zr}$ presents small grains (around 500 nm in size) while further away from the Cr the grains appear to be larger. Features resembling dislocation lines and bend fringes are found in the Laves phase grains, suggesting that some stress and strain are present, potentially induced during cooling. Box 1 presented in Fig. 6 shows one of the Zr-rich particles at higher magnification. The corresponding Pattern A was indexed as monoclinic zirconia. At this scale it is possible to reveal substructures: bands 50 nm wide stretch across the particle from side to side, possibly caused by tetragonal to monoclinic transformation occurring at 1043°C, with a 3% volume change [40], during cooling of the ZrO_2 -particles. The selected area diffraction pattern B was indexed as cubic C15-type Laves phase.

STEM imaging and STEM EDS were employed to obtain detailed chemical information about the composition of the $(\text{Cr,Fe})_2\text{Zr}$ Laves phase and the Zr-rich particles growing along the Cr-grain boundaries. In Fig. 7, STEM images of the Laves phase formed at the coating-substrate interface and of the Cr-coating are displayed, the Zr-substrate is not shown. The intermetallic microstructure is characterized by a grain size around 1–2 μm. Some plastic deformation seems to have occurred as suggested by the twin lines visible in Fig. 7, Box B. The formation of the twins is likely to be attributed to residual stresses induced into the material during the cooling. ZrO_2 particles are found very frequently decorating the grain boundaries of the recrystallized Cr coating. The table presented in Fig. 7 contains the chemical compositions of various areas on the analysed lamella obtained with STEM EDS point analysis. The measured composition of the Laves phase is the same throughout the entire layer and it agrees with the $(\text{Cr,Fe})_2\text{Zr}$ stoichiometry. An Fe content of 1–2 at.% is found in this phase, probably coming from the Zr substrate and substituting Cr in the Laves lattice. The composition of the Zr-rich particles is less uniform. The most common composition is Zr 30–35 at.% and O 64–70 at.%, compatible with ZrO_2 . The Cr content, though, can vary between 0 at.% and 6 at.% (with 20 at.% Cr, Point 11 seems to be an outlier, probably because of signal contribution from the matrix matrix). Where the lamella was the thinnest, almost no Cr was measured (between 0 at.% and 0.5 at.%), which would agree with the hypothesis of the matrix influencing the results for the particles measured in thicker regions. On the other hand, for all measured points (excluding Point 11), the O content is not diluted by Cr and it is constant at about 66 at.% or above, which would suggest that the Cr is actually part of

the ZrO_2 particles and that it can substitute Zr in the oxide chemistry. Point 9, in particular, seems to confirm this hypothesis, as the particle is relatively large, and contribution from the matrix seems to be less likely. The solubility of Cr_2O_3 in ZrO_2 is reported to be around 9–10 wt.% [41], the corresponding chemical composition calculated in atomic percentage corresponds to 29 at.% Zr, 66 at.% O and 5 at.% Cr, which fits reasonably well with the composition measured in Point 9 and Point 10, confirming the hypothesis of Cr dissolution in the ZrO_2 reasonable. STEM EDS line scans across the $(\text{Cr,Fe})_2\text{Zr}$ – Cr interface and across one of the ZrO_2 particles are plotted in Fig. 7c and 7d. Both interfaces appear to be sharp with little or no phase intermixing.

3.3. Microstructural evolution of the Cr-coating and coating-substrate interface

Cold spray deposition produces coatings with a characteristic microstructure: the high-rate, high-strain plastic deformation involved in particle collisions produces regions of small grains formed by dynamic recrystallization, typical of the material between two particles, and regions deformed but not recrystallized, typical of the former bulk of a sprayed particle [37]. These different regions are clearly visible in the first row of Fig. 8, presenting EBSD maps. In the as-fabricated material, large areas with the same grain orientation and only gradual crystal rotation due to deformation can be seen surrounded by a multitude of very small grains. Depending on the selected cross section, more or less of these two morphologies will be visible. After the exposure to PWR autoclave, the bulk of the former particles has experienced almost no relaxation or change in microstructure, while some degree of recrystallization has occurred in the very small grains found in the inter-particle areas [38]. In Fig. 8, the microstructure characteristic of the former bulk of the coating particles appears less frequent and more work-hardened in the case of the PWR autoclaved material, but this has only to do with local variations. When the material is tested in steam at 1200°C, the Cr-coating, already prone to recrystallization, goes through full thermal recrystallization within the first 3 min as shown in Fig. 8, achieving a final grain size ranging between 5 and 15 μm. Some smaller, 1–2 μm, grains can still be found in certain regions, but do not represent the general case. The microstructure observed in the coating after 20 min and 40 min does not show any significant modification or addi-

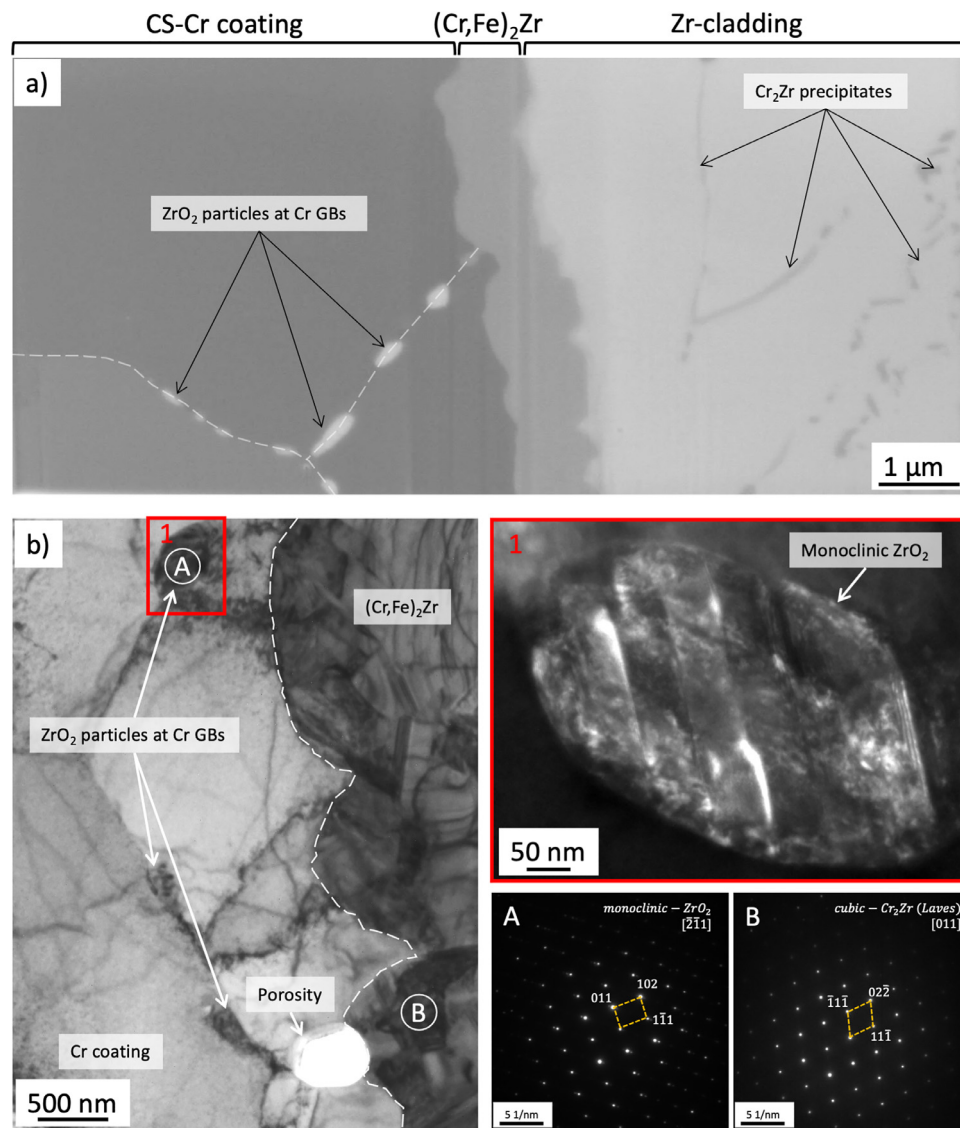


Fig. 6. CS Cr-coated OPZ cladding tubes exposed to LOCA condition (1200°C in steam) for 40 min. a) SEM image of FIB cross-section of the interface region between Cr-coating and Zr-substrate. (The white dashed line indicates grain boundaries of the recrystallized Cr.) b) BF-TEM image of the interface between $(\text{Cr,Fe})_2\text{Zr}$ and the Cr-coating after 40 min in LOCA conditions. Box 1: Detail of monoclinic ZrO_2 particle found at a Cr grain boundary. SAED Pattern A and Pattern B are collected from a ZrO_2 particle and a $(\text{Cr,Fe})_2\text{Zr}$ grain, respectively. (The white dashed line indicates the phase interface between Cr and $(\text{Cr,Fe})_2\text{Zr}$.)

tional change. Under these conditions, the coating is progressively oxidised, but no further recrystallization occurs. No preferred orientation or texture is observed to be developing in the coating. At the coating-substrate interface, 50 nm sized nuclei of $(\text{Cr,Fe})_2\text{Zr}$ Laves phase were found after PWR autoclave exposure [38], but they are not visible at this scale. After the first 3 min under simulated LOCA conditions, the Laves phase has grown to a thickness of around 0.5 μm and it is visible in the presented EBSD maps. For longer exposure times it grows slightly up to 1–2 μm in thickness. The most frequent grain structure is represented by 1 μm large grains that can stretch across the entire thickness of the layer, but smaller grains can also be found. No texture or preferred orientation is observed in the Laves grains.

4. Discussion

4.1. Cold spray Cr-coating: high temperature oxidation mechanisms

Cold sprayed Cr-coatings have been shown to work well under simulated PWR operating water chemistry conditions [4,7,10,38],

but the principal reason for their development and potential future deployment is the improved accident tolerance they can provide. In this work, the ability of CS-Cr coatings to survive severe accident conditions while protecting the underlying Zr-cladding was tested, and the coatings demonstrated good performance. The tested conditions are not identical to those a cladding tube would experience in a real accident (gas pressure from the inside, pellet cladding interaction, potentially longer exposure times, different temperature ramp-up, pre-oxidation during normal operation before the accident, effects of irradiation, and water quench once the cooling is restored), but the oxidation resistance shown in this test suggests that CS-Cr coatings is a promising option for ATF.

The oxide scale formation starts with an outward growth mechanism. As can be seen in Fig. 1, the chromia layer after 3 min of oxidation is very compact and no porosities are present in the scale. The oxide-coating interface is not continuous and points of contact can be found alternating with interfacial porosities. This morphology is typical of outward growth of the oxide fostered by outward diffusion of metal atoms [26]; as the chromia nucleates on the surface of the coating, Cr-vacancies are injected into the coat-

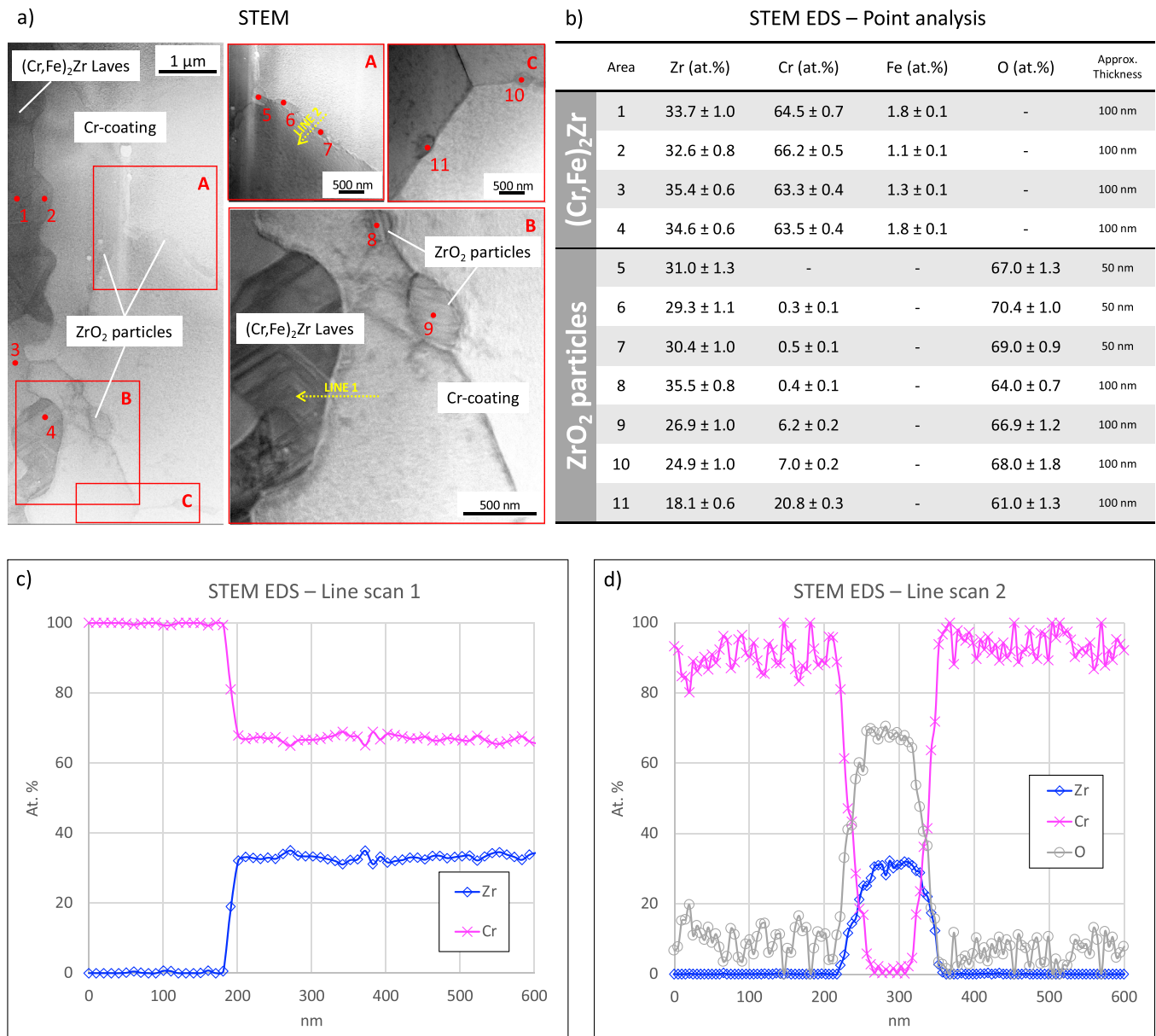


Fig. 7. (a) STEM images of CS Cr-coated OPZ cladding tubes exposed to LOCA condition (1200°C in steam) for 40 min: interface region between Cr-coating and Zr-substrate. (b) Results of STEM-EDS point analysis. Composition profiles obtained by STEM EDS. Line scan 1 and Line scan 2 are plotted in (c) and (d).

ing while Cr-atoms diffuse into the newly formed chromia grains through the oxide-metal interface. Bulk diffusion is generally orders of magnitude slower than surface diffusion. As a consequence, when the first chromia scale forms, vacancies will tend to condense as pores at the oxide-metal interface first [42], producing the oxide-metal interface shown in Fig. 1. After 20 min of oxidation, the oxide-metal interface is now continuous and less porosity can be found. Additionally, the oxide itself contains a porous band. The oxidation mechanism has transitioned to a mixed outward-inward growth mechanism. At this stage the scale thickness is acting as a barrier for Cr diffusion and it is more difficult for the Cr to reach the O on the outer surface of the scale. Oxygen at the scale surface captures Cr atoms to facilitate scale growth, resulting in what appears as a continuous injection of Cr-vacancies into the growing chromia from the outer surface. Oxygen diffusing through the scale, instead, will meet Cr atoms at the oxide-metal inter-

face and promote oxide growth into the metallic Cr. The inward growth is controlled by the amount of available oxygen, and the formed chromia is oxygen depleted which can be modelled as the injection of O-vacancies into the chromia from the oxide-metal interface [20–22]. The result is an outer layer of chromia with an excess of Cr-vacancies (p-type semiconductor), an inner layer of chromia with excess of O-vacancies (n-type semiconductor), and a mid-region where Schottky vacancy annihilation occurs, and void formation is observed. The non-uniform surface charge distribution and hence different electrostatic fields protruding out from the sample surface in the n-type and p-type regions is the main reason behind the SEM secondary electron contrast between the outer chromia subscale and the inner chromia subscale visible in Fig. 1. Because of this difference in the electrostatic fields, the secondary electrons emitted from the n-type regions of the sample surface, face an extra energy barrier to reach the energy level of

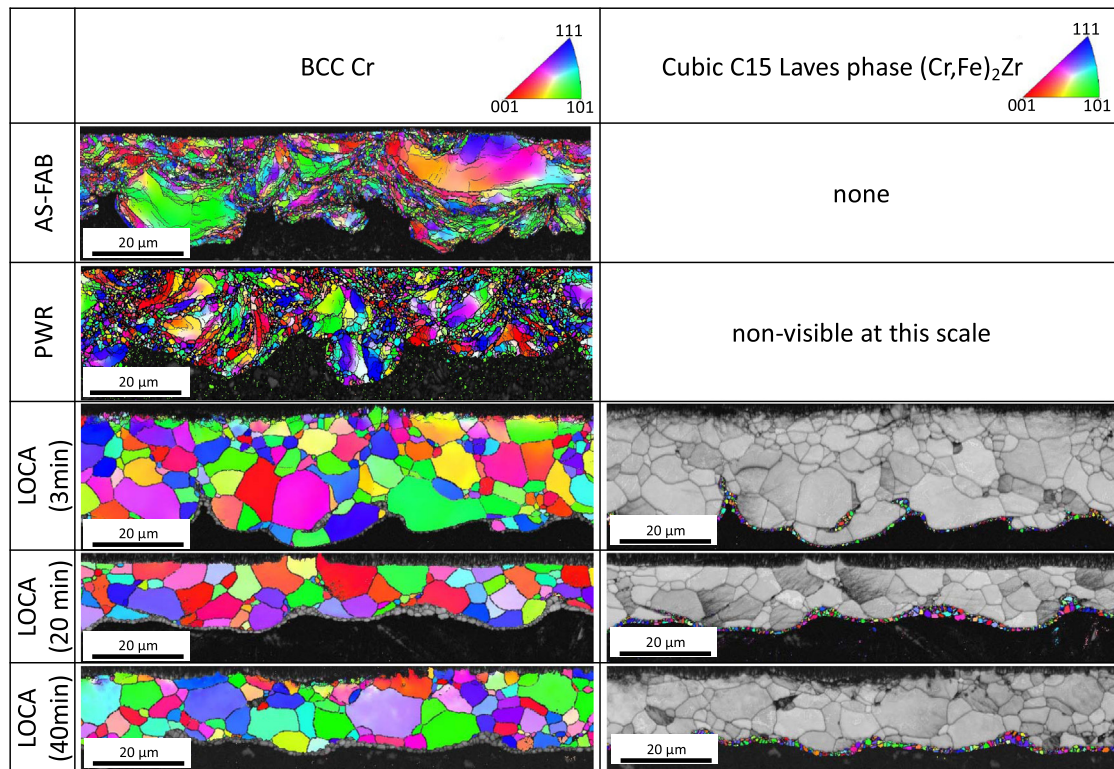


Fig. 8. EBSD cross-section maps of CS Cr-coated OPZ cladding tubes as-fabricated, exposed to PWR autoclave, and exposed to LOCA condition (1200°C in steam) for 3 min, 20 min and 40 min, respectively (in every map the Cr-coating is shown on top and the Zr-substrate at the bottom). Left column: Band contrast map + IPFz map for BCC Cr. Right column: Band contrast map + IPFz map for Cubic C15 Laves phase (Cr,Fe)₂Zr.

the vacuum inside the SEM chamber and be detected. Therefore, there will be more secondary electrons detected from the p-type regions, hence more signal and brighter contrast [43].

From the coatings point of view, Cr out-diffusion towards the scale will be necessary for oxide growth (injection of Cr vacancies), which leads to the accumulation of vacancies in the metallic Cr lattice and the appearance of Kirkendall porosities in the coating close to the oxide-metal interface, as seen in Fig. 3. The oxide growth follows a parabolic kinetics, as previously demonstrated in literature [5] and confirmed in this experiment by the decreasing growth rate seen between 3–20 min and 20–40 min time ranges (Fig. 2). No volatilization of the developed chromia scale was measured in this experiment, but it might occur after longer exposure times (tens of hours) [15]. The observed rate of oxidation of the coating represents a significant improvement when compared with uncoated Zr-claddings. As visible in Fig. 1, around 80 μm of ZrO₂ has grown on the uncoated inner wall of the cladding after 40 min LOCA exposure (around ten times thicker oxide than on the coated side). Similar values are reported for fully uncoated claddings [44] and claddings sealed at both ends to avoid oxidation from the inner wall [45], which allows to exclude any effect that would result in preferential oxidation of the uncoated side (i.e., Zr acting as sacrificial anode). As mentioned previously, this experiment does not fully reproduce real accident conditions, and three main differences need to be taken into consideration: pellet-cladding interaction, irradiation and pre-oxidation of the cladding during operation. In the real case, the cladding would have been in operation for a period of time before the accident, a thin layer of chromia is expected to form as suggested by the autoclave tests [38]. During operation, the cladding creeps down, comes in contact with the pellet and then follows the pellet expansion [46,47]. In addition, irradiation can change the oxidation rate of the cladding

and potentially the morphology of the oxide scale [48]. The pre-existence of a thin and compact oxide layer could be beneficial, passivating the metallic Cr and delaying oxidation of the coating, but without experimental tests it is difficult to tell what effects irradiation, creep and swelling could have on the coating oxidation rate in operation and consequently on coating performance during an accident.

4.2. Recrystallization of the cold spray Cr-coating

Cold spray deposited material is characterized by a high degree of plastic deformation. During deposition, the incoming particles hit the substrate surface (or previously deposited coating) at high velocity. Upon collision, high-rate, high-degree plastic deformation occurs, particularly in the periphery of the particles [32]. The resulting plastic flow allows to fill in gaps and to generate intimate contact between the incoming particle and the substrate or coating under formation. As a consequence, the final microstructure will contain a large amount of residual stress, high dislocation density, regions of very small grains and larger grains with significant deformation, as displayed in Fig. 8 [37]. A small degree of recrystallization is already observed after 90 days in PWR autoclave at the relatively low temperature of 415°C [38]. Hence, recrystallization occurring at 1200°C was expected and potentially desired as larger grains can offer a better barrier for grain boundary diffusion and might have some effect on the oxidation process [49]. In Fig. 8, it is possible to see a large degree of recrystallization happening after 3 min exposure under LOCA conditions. Here the grain size increases to around 5–15 μm, no obvious texture seems to have developed as the grains are mostly equiaxed, and no favoured lattice orientation has appeared. Some smaller grains can be found, generally above 1 μm in size. Grain size can have different effects on oxidation

depending on the oxidation mechanism. In the 1200–1600°C temperature range, Cr-self diffusion is not influenced by grain boundary diffusion anymore [50]. Additionally, the Kirkendall porosities, visible in Fig. 3, are found inside the Cr-grains, which further suggests that the density of Cr-grain boundaries should not have a direct effect on the oxidation of the Cr-coating. Nonetheless, ZrO_2 particles inside the coating could only be found at the grain boundaries of the recrystallized Cr. The nucleation of ZrO_2 particles and their growth into a network creating a path for O from the chromia scale to the Zr-substrate has been identified as one of the possible failure modes of Cr-coatings under simulated accident conditions [11]. Zr could not be measured inside the Cr-grains, and it is reasonable to assume that Zr atoms manage to penetrate the coating only along Cr grain boundaries. It is then clear that a lower density of grain boundaries in the coating should increase the protection offered by the coating under accident conditions. Nevertheless, once the network of ZrO_2 has formed and O is allowed to enter the Zr substrate, a lower density of grain boundaries could result in a more localized oxidation of the substrate, which could produce higher strains and be detrimental.

4.3. Evolution of the Cr-Zr interface: reaction and interdiffusion

The most evident phenomenon happening at the coating-substrate interface during LOCA exposure is the formation of a dense and continuous layer of $(\text{Cr,Fe})_2\text{Zr}$ cubic C15-type intermetallic Laves phase. The Laves phase seems to nucleate as pure Cr_2Zr , which is enriched over time with small amounts of Fe. Two versions of Cr_2Zr exist, a C15-type (cubic) low temperature phase and a C14-type (hexagonal) high temperature phase, the transition between the two is at 1592°C, so only the C15-type is expected in the studied material [39]. The Cr content of the C15-type phase can vary between 64 at.% and 69 at.% at 900°C [39], which fits with the measured composition of about 64 at.% of Cr plus 1–2 at.% of Fe. At 1200°C, up to 3–4 at.% Fe can substitute Cr in the Cr_2Zr intermetallic lattice without changing the crystal structure [51], but above this value the structure changes to C14-type, as Fe acts as a C14-type stabilizer. The Fe found in the C15-type Laves phase probably originates from the Zr-substrate. The OPZ contains small amounts of Fe (0.09–0.13 at.%), and this Fe is generally located in secondary phase particles (SPPs) distributed in the Zr-matrix in the form of C14-type Fe-rich Laves phase [52,53]. Fe is known to diffuse quite quickly in Zr (compared to Zr self-diffusion or Cr diffusion) [54], and the Fe enrichment in the layer of $(\text{Cr,Fe})_2\text{Zr}$ C15-type Laves phase found at the Cr-Zr interface must have occurred at the expense of the C14-type SPPs present in the Zr-matrix. Similar interactions between the Fe from the SPPs and the Laves phase present at the Cr-Zr interface have been discovered also in autoclave tested CS-Cr coated OPZ claddings [38]. In summary, this intermetallic is thermodynamically stable and it is expected to grow. Its nucleation at the interface was discovered even after PWR autoclave exposure at the relatively low temperature of 415°C for 90 days [38] and its presence is reported in many studies of similar systems and exposures [5,29,55,56]. This Laves phase is relatively brittle, but it does not seem to represent a point of failure: no spallation of the coating is seen, no significant concentration of cracks or porosities could be found in this area.

The growth of the intermetallic phase starts relatively quickly and it reaches 0.3–0.5 μm thickness after 3 min. It grows significantly between 3 min and 20 min up to around 1–1.5 μm thickness, then it seems to slow down, and little growth could be discerned between 20 min and 40 min exposure. Once formed, this intermetallic Laves phase will act as a diffusion barrier. It is reasonable to expect diffusion of Zr in the Laves phase to be 1–2 or-

ders of magnitude slower than the diffusion of Cr in the same lattice [57]. In fact, Cr is able to penetrate through the 1–2 μm thick Laves layer and progressively diffuse deeper into the Zr-cladding as demonstrated in Fig. 5, while the Zr content in the bulk of the Cr coating is measured to be zero (below the detection limit of about 0.1–0.2 at.%). Overall, the flux of Cr atoms to the Laves phase can become smaller than the flux of Cr atoms leaving the intermetallic to dissolve into the Zr substrate. This can inhibit growth of the $(\text{Cr,Fe})_2\text{Zr}$ Laves phase and even promote dissolution for longer exposure times, as reported in literature [56]. The grain size of the intermetallic Laves layer plays a role in controlling the diffusion of Zr to the Cr-coating. A thicker intermetallic layer, larger grains and lower density of grain boundaries could imply slower diffusion of Zr into the Cr-coating, delaying the formation of ZrO_2 particles in the coating (see Fig. 7) and the subsequent formation of the ZrO_2 network [11]. The presence of an intermixed bonding layer at the Cr-Zr interface in as-fabricated CS Cr-coated Zr-claddings, shown in previous studies [37,38], could play a role in the initial formation of the Laves phase. Ultimately, though, at these temperatures, the formation of the intermetallic phase is inevitable and will occur independently of the pre-existence of an intermixed bonding region or proto-nuclei. STEM images have shown the presence of twinning in the Laves layer, a sign of significant stresses in this phase, probably produced during cooling. In this work, the samples were cooled in air. A faster cooling, as in a post LOCA quench, could induce more severe stresses. Nonetheless, little or no spallation of the coating or of the oxide has been reported in literature for Cr-coatings quenched in water [11,45,56].

As mentioned before, Cr manages to diffuse quite freely through the Laves phase and can penetrate deep into the bulk of the cladding. The solubility of Cr in β -Zr at 1200°C is slightly above 5 at.% [39], this value is reached in the Zr adjacent to the coating and it decreases from there. The resulting Cr diffusion profile into the cladding produces regions with different alloying content. Depending on the Cr content, different phases can appear after quenching from the β -Zr field: precipitates of the metastable hexagonal ω phase with varying c/a ratios, precipitates of $(\text{Cr,Fe})_2\text{Zr}$ Laves phase, and laths of metastable α' phase (martensite) are the most commonly reported [39]. Cooling in air is slower than water quenching, but due to the very small volume of the exposed samples, it is still possible for these structures to form. Presence of Cr-rich precipitates in the cladding after exposure is evident, as shown in the box in Fig. 5 and in the SEM cross-section presented in Fig. 6. These precipitates, most likely $(\text{Cr,Fe})_2\text{Zr}$, have both lamellar and particle shapes depending on the region. In the EDS map presented in the box in Fig. 5, lath-shaped areas characterised by a high Cr signal can be found adjacent to regions containing Cr-rich precipitates but with lower Cr content in the matrix. For bulk diffusion of Cr in Zr crystal, the diffusion depths (d_{time}) measured for Cr into Zr after 3 min, 20 min, and 40 min depends on the diffusion lengths \sqrt{Dt} , where t is time and D is the diffusion coefficient. Because T is constant, the diffusion coefficient D can be considered constant as well. As a consequence, the diffusion depth should simply scale with \sqrt{t} . It is possible to verify this relationship by comparing the ratio between the measured diffusion depths at different times and the square root of the exposure time. Assuming the following experimental values for the diffusion depths of $d_{3 \text{ min}} \cong 75 \mu\text{m}$, $d_{20 \text{ min}} \cong 200 \mu\text{m}$, and $d_{40 \text{ min}} \cong 300 \mu\text{m}$ the ratios are calculated as follow: $75 \mu\text{m}/200 \mu\text{m} = 0.38$ and $\sqrt{3 \text{ min}}/\sqrt{20 \text{ min}} = 0.39$ which show excellent fit, $200 \mu\text{m}/300 \mu\text{m} = 0.67$ and $\sqrt{20 \text{ min}}/\sqrt{40 \text{ min}} = 0.71$ that show a good fit. The ratios calculated from the model and from the experimental data appear to match, which suggests that bulk diffusion of Cr in the Zr lattice from the Laves-Zr interface represents the main transport phenomenon.

4.4. Advantages and disadvantages of cold spray Cr-coatings

Different Cr-coatings are being developed for ATF applications. A large range of deposition technologies are being tested, but the most common techniques currently used to produce metallic Cr coatings are PVD and CS [30]. The most important characteristics of CS coating is the severely strained and deformed microstructure produced by the collisions of the particles during the coating process [32]. When dealing with high temperatures, as shown in Fig. 8, CS coatings recrystallize very quickly, as the very high degree of deformation and the high density of dislocations act as driving force for recrystallization and formation of new stress-free grains [58–60]. As discussed in the section about oxidation, larger Cr-grains can be considered an advantage under accident conditions. After only 3 min at 1200°C the CS Cr-coating has recrystallized into large 5–15 µm grains. The microstructure does not evolve significantly afterwards, and it can be considered fully recrystallized. As-fabricated PVD coatings are often characterized by grain size around 1 µm, often columnar or fibre-like, and textured with specific grain orientations aligned along the growth direction [12,61–63]. Full recrystallization of the Cr coating at elevated temperature (1000–1200°C) is reported for PVD Cr-coatings as well. This process occurs over similar time scales, but the final grain size is usually in the 1–5 µm range, and the preferred grain orientation can sometime be maintained [11,12,30,55].

Another difference between PVD and CS is the growth rate of the Laves phase, which is reported in literature to be slightly higher in the CS coating [56]. This is generally attributed to the ballistic surface cleaning that occurs in CS which is able to spall off the native oxide scale present on the Zr surface. The native oxide is usually very thin (5–20 nm [64]) but is deemed able to slow down the initial stages of interdiffusion in a diffusion couple [56]. Also, the Cr-Zr interface in the studied CS coating is characterized by the presence of a 10–20 nm thick intermixed bonding region where Zr and Cr are already mixed (60 at.% Zr, and 30 at. % Cr) [37]. This region is produced by a very localized heating that occurs during particle collision and it could represent a favourable place for the Laves phase to nucleate at the beginning of the interdiffusion. Faster growth rates of the Laves layer can be considered advantageous, as it reduces all diffusive processes between the coating and the cladding, which leads to slower dissolution of the coating into the cladding, slower diffusion of Zr into the Cr grain boundaries, and potentially longer effective protection offered by the coating. To better evaluate the actual significance of these differences for performance, future work on coatings with the same thickness, under identical experimental conditions would be needed. Moreover, experiments at intermediate temperatures (or with temperature ramps), and water quench, would reproduce even better the actual stresses and challenges faced by the coatings in an actual accident scenario.

5. Conclusions

Cr coatings deposited with CS technology were shown to effectively protect the Zr-substrate from oxidation under simulated LOCA conditions. After 40 min at 1200°C in flowing steam, an 8 µm thick chromia scale had formed on the outer surface of the Cr-coating. The oxidation kinetics followed a parabolic law and no significant spallation of the oxide scale could be observed. At the interface between the coating and the substrate, Cr and Zr reacted forming a (Cr,Fe)₂Zr Laves phase layer. This layer reached a maximum of 1.5–1.7 µm in thickness and seemed to have a role in slowing down the dissolution of the Cr coating into the Zr alloy. The microstructure of the coating, initially severely deformed, was fully recrystallized after the first 3 min of exposure. The obtained microstructure is characterized by large equiaxed grains 5–15 µm

in size. ZrO₂ particles were found nucleating and growing at the grain boundaries of the recrystallized Cr. As the Cr grain boundaries seem to be the main pathway for oxygen through the protective coating, the prompt coarsening of the CS-Cr grain structure can be considered beneficial. Particularly important in this regard is the tendency of the CS-Cr to recrystallize into large and equiaxed grains, 5–15 µm in size, that do not stretch across the whole coating. Because of this, the grain boundary density is very low and no grain boundary links the outer surface of the coating to the substrate, strongly reducing the amount of direct pathways for the O to diffuse towards the substrate. To further validate the effectiveness of this coating, testing CS-Cr coated claddings in autoclave or reactor before exposing it to simulated accident condition would be ideal, as irradiation and oxidation during operation could influence the morphology and microstructure of the system and change its performances during a severe accident. To identify or exclude any significant effect of the deposition method on the oxidation protection offered by Cr coatings during an accident, Cr-coatings of the same thickness, deposited using different techniques (e.g. CS and PVD), should be tested and characterized.

Declaration of Competing Interest

The authors declare that they have no known competing financial interests or personal relationships that could have appeared to influence the work reported in this paper.

CRediT authorship contribution statement

Andrea Fazi: Investigation, Writing – original draft, Visualization, Conceptualization. **Mohammad Sattari:** Investigation, Methodology. **Krystyna Stiller:** Writing – review & editing, Conceptualization. **Hans-Olof Andrén:** Writing – review & editing, Conceptualization. **Mattias Thuvander:** Supervision, Project administration, Funding acquisition, Writing – review & editing, Conceptualization.

Data availability

No data was used for the research described in the article.

Acknowledgements

This project is financially supported by the Swedish Foundation for Strategic Research (SSF) (Grant number: EM16-0031). Westinghouse Electric Sweden is acknowledged for providing the analysed samples. All the experimental work presented in this paper was performed at Chalmers Materials Analysis Laboratory (CMAL).

References

- [1] S.J. Zinkle, K.A. Terrani, J.C. Gehin, L.J. Ott, L.L. Snead, Accident tolerant fuels for LWRs: A perspective, *J. Nucl. Mater.* 448 (2014) 374–379, doi:10.1016/j.jnucmat.2013.12.005.
- [2] K.A. Terrani, Accident tolerant fuel cladding development: Promise, status, and challenges, *J. Nucl. Mater.* 501 (2018) 13–30, doi:10.1016/j.jnucmat.2017.12.043.
- [3] J.C. Brachet, M. le Saux, M. le Flem, S. Urvoy, E. Roues, T. Guilbert, C. Cobac, F. Lahogue, J. Rousselot, M. Tupin, P. Billaud, C. Hossepied, F. Schuster, F. Lomello, A. Billard, G. Velisa, E. Monsifrot, J. Bischoff, A. Ambard, On-going studies at CEA on chromium coated zirconium based nuclear fuel claddings for enhanced Accident Tolerant LWRs Fuel, in: *TopFuel*, 2015, pp. 31–38.
- [4] B. Maier, H. Yeom, G. Johnson, T. Dabney, J. Walters, P. Xu, J. Romero, H. Shah, K. Sridharan, Development of cold spray chromium coatings for improved accident tolerant zirconium-alloy cladding, *J. Nucl. Mater.* 519 (2019) 247–254, doi:10.1016/j.jnucmat.2019.03.039.
- [5] H. Yeom, B. Maier, G. Johnson, T. Dabney, M. Lenling, K. Sridharan, High temperature oxidation and microstructural evolution of cold spray chromium coatings on Zircaloy-4 in steam environments, *J. Nucl. Mater.* 526 (2019) 151737, doi:10.1016/j.jnucmat.2019.151737.
- [6] H.-G. Kim, I.-H. Kim, Y.-I. Jung, D.-J. Park, J.-H. Park, B.-K. Choi, Y.-H. Lee, Out-of-pile performance of surface-modified Zr cladding for accident tolerant fuel in LWRs, *J. Nucl. Mater.* 510 (2018) 93–99, doi:10.1016/j.jnucmat.2018.07.061.

- [7] M. Ševeček, A. Gurgun, A. Seshadri, Y. Che, M. Wagih, B. Phillips, V. Champagne, K. Shirvan, Development of Cr cold spray-coated fuel cladding with enhanced accident tolerance, *Nuclear Engineering and Technology* 50 (2018) 229–236, doi:[10.1016/j.net.2017.12.011](https://doi.org/10.1016/j.net.2017.12.011).
- [8] M. Wagih, B. Spencer, J. Hales, K. Shirvan, Fuel performance of chromium-coated zirconium alloy and silicon carbide accident tolerant fuel claddings, *Ann. Nucl. Energy* 120 (2018) 304–318, doi:[10.1016/j.anucene.2018.06.001](https://doi.org/10.1016/j.anucene.2018.06.001).
- [9] J. Hazan, A. Gauthier, E. Pouillier, K. Shirvan, Semi-integral LOCA test of cold-spray chromium coated zircaloy-4 accident tolerant fuel cladding, *J. Nucl. Mater.* 550 (2021) 152940, doi:[10.1016/j.jnucmat.2021.152940](https://doi.org/10.1016/j.jnucmat.2021.152940).
- [10] R.v. Umretiya, B. Elward, D. Lee, M. Anderson, R.B. Rebak, J.v. Rojas, Mechanical and chemical properties of PVD and cold spray Cr-coatings on Zircaloy-4, *J. Nucl. Mater.* 541 (2020) 152420, doi:[10.1016/j.jnucmat.2020.152420](https://doi.org/10.1016/j.jnucmat.2020.152420).
- [11] J.C. Brachet, E. Rouesne, J. Ribis, T. Guilbert, S. Urvoy, G. Nony, C. Toffolon-Masclet, M. le Saux, N. Chaabane, H. Palancher, A. David, J. Bischoff, J. Augereau, E. Pouillier, High temperature steam oxidation of chromium-coated zirconium-based alloys: Kinetics and process, *Corros. Sci.* 167 (2020) 108537, doi:[10.1016/j.corsci.2020.108537](https://doi.org/10.1016/j.corsci.2020.108537).
- [12] Y. Wang, L. Wang, L. Shang, G. Bai, J. Li, F. Xue, W. Gong, Fiber texture-dependent oxidation behaviour of Cr-coated zirconium alloy in high temperature steam, *Corros. Sci.* 205 (2022) 110449, doi:[10.1016/j.corsci.2022.110449](https://doi.org/10.1016/j.corsci.2022.110449).
- [13] H. Yeom, B.R. Maier, G. Johnson, K. Sridharan, Cold Spray Coatings for Accident Tolerant Zr-Alloy Cladding in Light Water Reactors, in: *Trans Am Nucl Soc.* 2018, pp. 1576–1579. <https://www.researchgate.net/publication/325812110>.
- [14] H. Asteman, J.E. Svensson, L.G. Johansson, M. Norell, Indication of chromium oxide hydroxide evaporation during oxidation of 304L at 873 K in the presence of 10% water vapor, *Oxid. Met.* 52 (1999) 95–111, doi:[10.1023/a:1018875024306](https://doi.org/10.1023/a:1018875024306).
- [15] N.K. Othman, N. Othman, J. Zhang, D.J. Young, Effects of water vapour on isothermal oxidation of chromia-forming alloys in Ar/O₂ and Ar/H₂ atmospheres, *Corros. Sci.* 51 (2009) 3039–3049, doi:[10.1016/j.corsci.2009.08.032](https://doi.org/10.1016/j.corsci.2009.08.032).
- [16] S. Tuzi, K. Göransson, S.M.H. Rahman, S.G. Eriksson, F. Liu, M. Thuvander, K. Stiller, Oxide evolution on Alloy X-750 in simulated BWR environment, *J. Nucl. Mater.* 482 (2016) 19–27, doi:[10.1016/j.jnucmat.2016.09.026](https://doi.org/10.1016/j.jnucmat.2016.09.026).
- [17] S. Tuzi, H. Lai, K. Göransson, M. Thuvander, K. Stiller, Corrosion of pre-oxidized nickel alloy X-750 in simulated BWR environment, *J. Nucl. Mater.* 486 (2017) 350–360, doi:[10.1016/j.jnucmat.2017.01.051](https://doi.org/10.1016/j.jnucmat.2017.01.051).
- [18] W.G. Cook, R.P. Olive, Pourbaix diagrams for chromium, aluminum and titanium extended to high-subcritical and low-supercritical conditions, *Corros. Sci.* 58 (2012) 291–298, doi:[10.1016/j.corsci.2012.02.002](https://doi.org/10.1016/j.corsci.2012.02.002).
- [19] B. Beverskog, I. Puigdomenech, Revised pourbaix diagrams for chromium at 25–300°C, *Corros. Sci.* 39 (1997) 43–57, doi:[10.1016/S0010-938X\(97\)89244-X](https://doi.org/10.1016/S0010-938X(97)89244-X).
- [20] M. Metikoš-Huković, M. Ceraj-Cerić, p-Type and n-Type Behavior of Chromium Oxide as a Function of the Applied Potential, *J. Electrochem. Soc.* 134 (1987) 2193–2197, doi:[10.1149/1.2100850](https://doi.org/10.1149/1.2100850).
- [21] L. Latu-Romain, Y. Parsa, S. Mathieu, M. Vilasi, Y. Wouters, Chromia Scale Thermally Grown on Pure Chromium Under Controlled p(O₂) Atmosphere: II—Spallation Investigation Using Photoelectrochemical Techniques at a Microscale, *Oxidation of Metals* 90 (2018) 267–277, doi:[10.1007/s11085-018-9848-3](https://doi.org/10.1007/s11085-018-9848-3).
- [22] L. Latu-Romain, Y. Parsa, S. Mathieu, M. Vilasi, M. Ollivier, A. Galerie, Y. Wouters, Duplex n- and p-Type Chromia Grown on Pure Chromium: A Photoelectrochemical and Microscopic Study, *Oxid. Met.* 86 (2016) 497–509, doi:[10.1007/s11085-016-9648-6](https://doi.org/10.1007/s11085-016-9648-6).
- [23] R.P. Oleksak, M. Kapoor, Daniel E. Perea, G.R. Holcomb, Ö.N. Doğan, The role of metal vacancies during high-temperature oxidation of alloys, *Npj Materials Degradation* 2 (1) (2018) 1–8 20182, doi:[10.1038/s41529-018-0046-1](https://doi.org/10.1038/s41529-018-0046-1).
- [24] B. Pujilaksono, T. Jonsson, M. Halvarsson, I. Panas, J.-E. Svensson, L.-G. Johansson, Paraline Oxidation of Chromium in O₂ + H₂O Environment at 600–700°C, *Oxid. Met.* 70 (2008) 163–188, doi:[10.1007/s11085-008-9114-1](https://doi.org/10.1007/s11085-008-9114-1).
- [25] S. Hallström, M. Halvarsson, L. Höglund, T. Jonsson, J. Ågren, High temperature oxidation of chromium: Kinetic modeling and microstructural investigation, *Solid State Ion* 240 (2013) 41–50, doi:[10.1016/j.ssi.2013.02.017](https://doi.org/10.1016/j.ssi.2013.02.017).
- [26] S. Henry, J. Mougín, Y. Wouters, J.P. Petit, A. Galerie, Characterization of chromia scales grown on pure chromium in different oxidizing atmospheres, *Mater. High Temp.* 17 (2000) 231–234, doi:[10.1179/mht.2000.17.2.008](https://doi.org/10.1179/mht.2000.17.2.008).
- [27] D. Caplan, M. Cohen, The Volatilization of Chromium Oxide, *J. Electrochem. Soc.* 108 (1961) 438, doi:[10.1149/1.2428106](https://doi.org/10.1149/1.2428106).
- [28] S. Mahboubi, H.S. Zurob, G.A. Botton, J.R. Kish, Effect of water vapour partial pressure on the chromia (Cr₂O₃)-based scale stability, *Can. Metall. Q.* 57 (2018) 89–98, doi:[10.1080/00084433.2017.1373968](https://doi.org/10.1080/00084433.2017.1373968).
- [29] J. Bischoff, C. Delafoay, N. Chaari, C. Vauglin, K. Buchanan, P. Barberis, E. Mon-sifrot, J.-C.B.F. Schuster, K. Nimishakavi, Cr coated cladding Development At Framatome, *TopFuel* (2018) 1–7.
- [30] J. Ko, J.W. Kim, H.W. Min, Y. Kim, Y.S. Yoon, Review of manufacturing technologies for coated accident tolerant fuel cladding, *J. Nucl. Mater.* 561 (2022) 153562, doi:[10.1016/j.jnucmat.2022.153562](https://doi.org/10.1016/j.jnucmat.2022.153562).
- [31] H. Yeom, K. Sridharan, Cold spray technology in nuclear energy applications: A review of recent advances, *Ann. Nucl. Energy* 150 (2021) 107835, doi:[10.1016/j.anucene.2020.107835](https://doi.org/10.1016/j.anucene.2020.107835).
- [32] P. Cavaliere, Cold-Spray Coatings: Recent Trends and Future perspectives, Springer, 2017, doi:[10.1007/978-3-319-67183-3](https://doi.org/10.1007/978-3-319-67183-3).
- [33] A. G2-88(2002), Standard Test Method for Corrosion Testing of Products of Zirconium, Hafnium, and Their Alloys in Water at 680°F or in Steam at 750°F, 88 (1988) 1–8. doi:[10.1520/G0002-88R02](https://doi.org/10.1520/G0002-88R02).
- [34] K. Thompson, D. Lawrence, D.J. Larson, J.D. Olson, T.F. Kelly, B. Gorman, In situ site-specific specimen preparation for atom probe tomography, *Ultramicroscopy* 107 (2007) 131–139, doi:[10.1016/j.ultramic.2006.06.008](https://doi.org/10.1016/j.ultramic.2006.06.008).
- [35] R.M. Langford, M. Rogers, In situ lift-out: Steps to improve yield and a comparison with other FIB TEM sample preparation techniques, *Micron* 39 (2008) 1325–1330, doi:[10.1016/j.micron.2008.02.006](https://doi.org/10.1016/j.micron.2008.02.006).
- [36] E.B. Kashkarov, D.V. Sidelev, M.S. Syrtanov, C. Tang, M. Steinbrück, Oxidation kinetics of Cr-coated zirconium alloy: Effect of coating thickness and microstructure, *Corros. Sci.* 175 (2020), doi:[10.1016/j.corsci.2020.108883](https://doi.org/10.1016/j.corsci.2020.108883).
- [37] A. Fazi, H. Aboulfadi, A.H.S. Iyer, M. Sattari, K.M. Stiller, P. Lokhande, M. Thuvander, H.O. Andren, Characterization of as-deposited cold sprayed Cr-coating on Optimized ZIRLO™ claddings, *J. Nucl. Mater.* 549 (2021) 152892, doi:[10.1016/j.jnucmat.2021.152892](https://doi.org/10.1016/j.jnucmat.2021.152892).
- [38] A. Fazi, K. Stiller, H.-O. Andren, M. Thuvander, Cold sprayed Cr-coating on Optimized ZIRLO™ claddings: the Cr/Zr interface and its microstructural and chemical evolution after autoclave corrosion testing, *J. Nucl. Mater.* 560 (2022) 153505, doi:[10.1016/j.jnucmat.2022.153505](https://doi.org/10.1016/j.jnucmat.2022.153505).
- [39] D. Arias, J.P. Abriata, The Cr-Zr (Chromium-Zirconium) System, *Bulletin of Alloy Phase Diagrams* 7 (1986) 237–245.
- [40] M. Allahkarami, J.C. Hanan, Mapping the tetragonal to monoclinic phase transformation in zirconia core dental crowns, *Dent. Mater.* 27 (2011) 1279–1284, doi:[10.1016/j.dental.2011.09.004](https://doi.org/10.1016/j.dental.2011.09.004).
- [41] D.A. Jerebtsov, G.G. Mikhailov, S.v. Sverdina, Phase diagram of the system: ZrO₂-Cr₂O₃, *Ceram. Int.* 27 (2001) 247–250, doi:[10.1016/S0272-8842\(00\)00071-7](https://doi.org/10.1016/S0272-8842(00)00071-7).
- [42] M.J. Graham, D. Caplan, R.J. Hussey, The Effect of Oxide Grain Structure on the High-Temperature Oxidation of Fe, Ni and Cr, *Can. Metall. Q.* 18 (1979) 283–291, doi:[10.1179/cm.1979.18.3.283](https://doi.org/10.1179/cm.1979.18.3.283).
- [43] C.P. Sealy, M.R. Castell, P.R. Wilshaw, Mechanism for secondary electron dopant contrast in the SEM, *J. Electron Microsc.* (Tokyo) 49 (2000) 311–321, doi:[10.1093/oxfordjournals.jmicro.a023811](https://doi.org/10.1093/oxfordjournals.jmicro.a023811).
- [44] M. Steinbrück, N. Vér, M. Große, Oxidation of Advanced Zirconium Cladding Alloys in Steam at Temperatures in the Range of 600–1200°C, *Oxid. Met.* 76 (2011) 215–232, doi:[10.1007/s11085-011-9249-3](https://doi.org/10.1007/s11085-011-9249-3).
- [45] M. Steinbrück, U. Stegmaier, M. Große, L. Czerniak, E. Lahoda, R. Daum, K. Yueh, High-temperature oxidation and quenching of chromium-coated zirconium alloy ATF cladding tubes with and w/o pre-damage, *J. Nucl. Mater.* 559 (2022) 153470, doi:[10.1016/j.jnucmat.2021.153470](https://doi.org/10.1016/j.jnucmat.2021.153470).
- [46] S. Suman, M.K. Khan, M. Pathak, R.N. Singh, Effects of hydrogen on thermal creep behaviour of Zircaloy fuel cladding, *J. Nucl. Mater.* 498 (2018) 20–32, doi:[10.1016/j.jnucmat.2017.10.015](https://doi.org/10.1016/j.jnucmat.2017.10.015).
- [47] K.L. Murty, Creep studies for zircaloy life prediction in water reactors, *JOM* 51 (1999) 32–39, doi:[10.1007/s11837-999-0184-6](https://doi.org/10.1007/s11837-999-0184-6).
- [48] A.T. Motta, A. Couet, R.J. Comstock, Corrosion of Zirconium Alloys Used for Nuclear Fuel Cladding, *Annu. Rev. Mater. Res.* 45 (2015) 311–343, doi:[10.1146/annurev-matsci-070214-020951](https://doi.org/10.1146/annurev-matsci-070214-020951).
- [49] K.D. Ralston, N. Birbilis, Effect of grain size on corrosion: A review, *Corrosion* 66 (2010) 0750051–07500513, doi:[10.5006/1.3462912](https://doi.org/10.5006/1.3462912).
- [50] J. Askill, D.H. Tomlin, Self-diffusion in chromium, *Philos. Mag.* 11 (1965) 467–474, doi:[10.1080/14786436508224234](https://doi.org/10.1080/14786436508224234).
- [51] Y. Yang, L. Tan, H. Bei, J.T. Busby, Thermodynamic modeling and experimental study of the Fe–Cr–Zr system, *J. Nucl. Mater.* 441 (2013) 190–202, doi:[10.1016/j.jnucmat.2013.05.061](https://doi.org/10.1016/j.jnucmat.2013.05.061).
- [52] A. Harte, M. Topping, P. Frankel, D. Jädnäs, J. Romero, L. Hallstadius, E.C. Darby, M. Preuss, Nano-scale chemical evolution in a proton-and neutron-irradiated Zr alloy, *J. Nucl. Mater.* 487 (2017) 30–42, doi:[10.1016/j.jnucmat.2017.01.049](https://doi.org/10.1016/j.jnucmat.2017.01.049).
- [53] G. Yuan, G. Cao, Q. Yue, L. Yang, Y. Yun, G. Shao, J. Hu, Formation and fine-structures of nano-precipitates in ZIRLO, *J. Alloys Compd.* 687 (2016) 451–457, doi:[10.1016/j.jallcom.2016.06.131](https://doi.org/10.1016/j.jallcom.2016.06.131).
- [54] R.v. Patil, G.P. Tiwari, B.D. Sharma, Self-diffusion in Zr–Cr and Zr–Fe alloys, *Philosophical Magazine A: Physics of Condensed Matter, Structure, Defects and Mechanical Properties* 44 (1981) 717–733, doi:[10.1080/01418618108236174](https://doi.org/10.1080/01418618108236174).
- [55] J.-C. Brachet, I. Idarraga-Trujillo, M.Le Flem, M.Le Saux, V. Vandenberghe, S. Urvoy, E. Rouesne, T. Guilbert, C. Toffolon-Masclet, M. Tupin, C. Phalip-pou, F. Lomello, F. Schuster, A. Billard, G. Velisa, C. Ducros, F. Sanchette, Early studies on Cr-Coated Zircaloy-4 as enhanced accident tolerant nuclear fuel claddings for light water reactors, *J. Nucl. Mater.* 517 (2019) 268–285, doi:[10.1016/j.jnucmat.2019.02.018](https://doi.org/10.1016/j.jnucmat.2019.02.018).
- [56] J. Yang, U. Stegmaier, C. Tang, M. Steinbrück, M. Große, S. Wang, H.J. Seifert, High temperature Cr-Zr interaction of two types of Cr-coated Zr alloys in inert gas environment, *J. Nucl. Mater.* 547 (2021) 152806, doi:[10.1016/j.jnucmat.2021.152806](https://doi.org/10.1016/j.jnucmat.2021.152806).
- [57] H. Martin, H. Helmut, Diffusion in the c15-type intermetallic laves phase NbCo₂, *Philosophical Magazine A: Physics of Condensed Matter, Structure, Defects and Mechanical Properties* 80 (2000) 1245–1263, doi:[10.1080/01418610008212113](https://doi.org/10.1080/01418610008212113).
- [58] I. Toda-Caraballo, J. Chao, L.E. Lindgren, C. Capdevila, Effect of residual stress on recrystallization behavior of mechanically alloyed steels, *Scr. Mater.* 62 (2010) 41–44, doi:[10.1016/j.scriptamat.2009.09.023](https://doi.org/10.1016/j.scriptamat.2009.09.023).

- [59] B. Marzbanrad, H. Jahed, E. Toyserkani, On the evolution of substrate's residual stress during cold spray process: A parametric study, *Mater. Des.* 138 (2018) 90–102, doi:[10.1016/j.matdes.2017.10.062](https://doi.org/10.1016/j.matdes.2017.10.062).
- [60] A.C. Hall, D.J. Cook, R.A. Neiser, T.J. Roemer, D.A. Hirschfeld, The effect of a simple annealing heat treatment on the mechanical properties of cold-sprayed aluminum, *J. Therm. Spray Technol.* 15 (2006) 233–238, doi:[10.1361/105996306X108138](https://doi.org/10.1361/105996306X108138).
- [61] J. Ribis, A. Wu, J.-C. Brachet, F. Barcelo, B. Arnal, Atomic-scale interface structure of a Cr-coated Zircaloy-4 material, *J. Mater. Sci.* 53 (2018) 9879–9895, doi:[10.1007/s10853-018-2333-1](https://doi.org/10.1007/s10853-018-2333-1).
- [62] J. Kabátová, F. Manoch, J. Kočí Ujp Praha, A.S. Praha-Zbraslav, L. Cvrček, J. Málek, S. Krum Ctú, In Prague, *Experimental Behavior of Chromium-Based Coatings*, *TopFuel* 156 (2018) A0233 2018.
- [63] B.O. Postolnyi, J.P. Araujo, Structural analysis of Arc-PVD multilayer metal nitride coatings CrN/MoN using electron backscatter diffraction (EBSD), 2016 International Conference on Nanomaterials: Application & Properties (NAP), IEEE, 2016 01NTF16-1-01NTF16-4, doi:[10.1109/NAP.2016.7757249](https://doi.org/10.1109/NAP.2016.7757249).
- [64] B. Wadman, H.-O. Andren, L.K.L. Falk, Atom Probe Analysis of Thin Oxide Layers on Zircaloy Needles, *Le Journal de Physique Colloques* 50 (1989) C8-303-C8-308, doi:[10.1051/jphyscol:1989851](https://doi.org/10.1051/jphyscol:1989851).